



CHORUS

This is the accepted manuscript made available via CHORUS. The article has been published as:

Electrically Driven Nonreciprocity Induced by Interband Photonic Transition on a Silicon Chip

Hugo Lira, Zongfu Yu, Shanhui Fan, and Michal Lipson
Phys. Rev. Lett. **109**, 033901 — Published 16 July 2012

DOI: [10.1103/PhysRevLett.109.033901](https://doi.org/10.1103/PhysRevLett.109.033901)

Electrically-driven non-reciprocity induced by inter-band photonic transition on a silicon chip

Hugo Lira¹, Zongfu Yu², Shanhui Fan², Michal Lipson^{3*}

¹ *School of Electrical and Computer Engineering, Cornell University, Ithaca, NY 14853, USA*

² *Department of Electrical Engineering, Stanford University, Stanford, California 94305, USA*

³ *Kavli Institute at Cornell for Nanoscale Science, Cornell University, Ithaca, NY 14853, USA*

*To whom the correspondence should be addressed. Email: michal.lipson@cornell.edu

We demonstrate an electrically-driven non-reciprocity on a silicon chip. By achieving an indirect interband photonic transition, we show that the transmission coefficients between two single-mode waveguides become dependent on the propagation directions only in the presence of the electrical drive. Our structure is characterized by a non-symmetric scattering matrix identical to a linear magneto-optical device.

The vast majority of photonic structures are reciprocal. Breaking reciprocity or time-reversal symmetry, as is typically accomplished with magneto-optical effects driven by external or internal magnetic fields, results in new physics such as the emergence of topologically protected one-way photonic edge modes¹⁻³, as well as a variety of important devices including circulators and isolators, all of which are described by a non-symmetric scattering matrix⁴. Unfortunately, magneto-optical effect is not present in standard optoelectronic materials including most metals and semiconductors. While non-magnetic approaches for achieving optical non-reciprocity have been extensively studied, the experimentally demonstrated approaches thus far however are either nonlinear or introduce additional frequency components. These approaches therefore have not completely reproduced a magneto-optical effect, which is linear and where the input and output waves have the same frequency. In this Letter, we demonstrate an electrically-driven non-reciprocity on a silicon chip. By achieving an indirect interband photonic transition⁵⁻⁶, we show that the transmission coefficients between two single-mode waveguides become dependent on the propagation directions only in the presence of the electrical drive. Importantly, our structure is characterized by a non-symmetric scattering matrix identical to a linear magneto-optical device.

There have been many previous efforts⁶⁻¹⁴ aiming to demonstrate optical non-reciprocity without using magneto-optical effects. These efforts complement the substantial recent progresses¹⁵⁻¹⁹ in miniaturization and integration of magneto-optical devices, by greatly broadening the choice of materials that can be used for demonstrating non-reciprocal physics. By the Lorentz reciprocity theorem, any linear system described by symmetric

and time-independent permittivity and permeability tensors are necessarily reciprocal²⁰. Therefore, to achieve non-reciprocity without magneto-optics one necessarily has to rely upon either non-linear or time-dependent effects. Non-reciprocity based upon both $\chi^{(2)}$, $\chi^{(3)}$ and parametric nonlinearity have been previously demonstrated^{7, 12-13}. In these nonlinear devices, however, non-reciprocity is power dependent. Thus, their behaviors cannot be characterized by a linear scattering matrix and are fundamentally different from magneto-optical devices. Alternatively, linear non-reciprocity that is independent of signal intensity has been experimentally observed in dynamic structures undergoing electrical modulation^{9, 11}. However, in all previously demonstrated electrically driven structures, the existence of non-reciprocity is associated with significant modulation frequency sidebands^{9, 11}, which again distinguish these devices from magneto-optical effects. While in principle acoustic-optic modulation can result in non-reciprocity, the low acoustic optic modulation frequency in the KHz to MHz frequency range results in a weak non-reciprocity that can be detected only with very long propagation distances²¹.

In this paper we present an experimental observation of non-reciprocity using interband photonic transition in a silicon waveguide. Photonic transitions in highly confined optical structures, where modes can be carefully manipulated and tailored, are of fundamental interests due to conceptual analogy with electronic transitions in semiconductors⁵. An indirect interband photonic transition occurs between two optical modes having different longitudinal wavevectors (hence the word “indirect”), and having transverse modal profiles with different symmetries (hence the word “interband” since the two modes belong to different photonic bands). Most photonic transitions, including the recent observation of photonic transition in micro-ring resonators²², and photonic transitions in

conventional travelling-wave electro-absorption modulators, are intraband transition between two modes with the same transverse modal profiles. In intraband transition, the modulation that provides phase-matched coupling between two modes at (ω, k) and $(\omega + \Delta\omega, k + \Delta k)$ will necessarily provide phase-matched coupling between the modes at $(\omega + \Delta\omega, k + \Delta k)$ and $(\omega + 2\Delta\omega, k + 2\Delta k)$. Thus there is always a cascade of transitions with associated frequency side bands. As a result, the demonstrated modulation-based isolation schemes always have significant frequency components in its output that is different from the input wave frequency. For demonstrating non-reciprocity, interband transition is more attractive since non-reciprocity occurs without the associated frequency side bands in the intra-band transition^{6, 13}.

Demonstrating indirect interband transition is however more challenging. Interband transitions between two different polarizations²¹ as can be achieved in acoustic optic modulators, have extremely small operation bandwidth due to the lack of group velocity matching between the two polarizations. In a waveguide system, to induce an interband transition between two modes with different symmetry in its transverse modal profile, the modulation itself cannot be uniform across the waveguide cross-section. In addition, since the typical frequency of high speed modulators²² is on the order of few GHz, the wavevector difference, between two different transverse modes having frequencies separated by a few GHz, is typically quite large and hence the modulation needs to be specifically constructed. Conventional travelling-wave electro-optic modulator design cannot generate such a large required modulation wavevector.

Here we demonstrate indirect interband photonic transitions in a slotted waveguide shown in Fig. 1a. The waveguide supports an even and an odd optical modes (Fig. 1a).

The dispersion relation of the waveguide, as shown in Fig. 1b, is tailored so that the two modes are separated in frequency by only a few GHz, for a difference in wavevector $k=2\pi/\lambda$ where λ is on the order of a few hundreds of microns. This enables one to create interband transition between the two modes by applying an electrical signal with a GHz frequency that is achievable in silicon electro-optic devices²³, and to use a structure that is compact (on the order of a few hundred microns in length). In order to induce photonic transition, the overlap integral between the modulation spatial distribution and the initial and final modes should be non zero⁶ and therefore in the simulation the modulation is applied only to half of the slotted waveguide. Non-reciprocity in such structure is achieved, since the photonic transition does not occur when light propagates in the forward direction from left to right, and occurs only when light propagates in the opposite backward direction (Fig. 1b). For this structure, assuming dimensions $w=450\text{nm}$, $h=215\text{nm}$, $t=35\text{nm}$ and $d=500\text{nm}$, Figure 1c shows the mode amplitudes in both directions using coupled mode equations⁶, for a continuous wave input when the structure is subject to a 10 GHz index modulation. One sees total conversion in the backward direction and minimal conversion ($<2\%$ in the example shown) in the forward direction. We emphasize that both the modulation and the optical input are continuous wave (CW). The observed non-reciprocity is completely independent of the relative timing between the optical signal and the modulation.

The most unambiguous demonstration of non-reciprocity is to observe an asymmetry in the transmission coefficients between two *single-mode* waveguides for the forward and backward transmission directions. We therefore place 1x2 MMI (Multi-Mode Interference waveguide) on both ends of the slotted waveguide (Fig. 2a). The MMI

serves to couple between a single mode waveguide (with an even mode) and the even mode of the slotted waveguide, and to filter away the converted odd mode.

We contrast the two cases where we inject light into the single mode waveguides along the two directions with the slotted waveguide undergoing modulation that induces interband transition. Fig. 2b shows a 2D time-domain FEM (Finite Element Method) simulation of the structure demonstrating such a contrast. In the forward direction (left to right), the photonic transition is not allowed, and the mode remains even in the slotted waveguide (Fig. 2b, top panel). Thus the structure has a high transmission coefficient. In contrast, in the backward direction (right to left), the transition is allowed and therefore the even mode injected into the slotted waveguide is completely converted to the odd mode, which is filtered away by the MMI (Fig. 2b, bottom panel). As a result, the structure has a low transmission coefficient in the backward direction.

We note that in Fig. 2b the converted light, which is at a frequency that is slightly different from the input, is completely radiated away by the MMI. Since the conversion occurs along only one direction, the use of MMI results in a direction-dependent loss that is non-reciprocal. The waves in the two single mode waveguides only have a single frequency component that is the input frequency. As a result, as far as the wave in the two single mode waveguides is concerned, the structure is completely characterized by a single 2×2 scattering matrix with directional-dependent transmission coefficients. From the scattering matrix perspective the structure is therefore indistinguishable from a magneto-optical device. None of the previous demonstrated non-reciprocal structures that do not use magneto-optical effects have this property.

Based on the theory and numerical simulations above, we experimentally demonstrate the non-reciprocity in interband photonic transition in this system. We place pn-junction electrical diodes inside a slotted waveguide, and realize electrical traveling wave modulation by applying voltages to these diodes through two microwave transmission lines. We use a modulation frequency of 10GHz, which corresponds to the difference in frequency between the two optical modes for the waveguide shown in Fig. 1b above. At this modulation frequency, the electrical wave along the transmission lines has a large period above a centimeter and a corresponding small wavevector, which is not suitable for achieving the interband transition that we require here.

To achieve a larger modulation wavevector, in our structure, the modulation wavevector is instead encoded in the pn-junction configurations. We use an array of two different junction regions (pn-np and np-pn) placed in alternating positions along the waveguide, and sinusoidally varying the voltages in the two transmission lines with a $\pi/2$ difference, as shown in Fig. 3a and Fig. 3b. Under an applied bias, only the reverse-biased diodes experience carrier depletion and hence generate significant index change, while the forward-biased diodes experience only minimal carrier leakage and generate no significant index change. In this way, we therefore create a traveling wave refractive index modulation profile, with a spatial period corresponding to four junction regions along the waveguide (Fig. 3c). Our configuration of junction regions also ensures that index modulation is induced in part of the cross section of the waveguide, fulfilling the required condition of non-zero overlap between the modulation and the product of the profiles of the modes involved.

The achieved modulation of the refractive index along the waveguide is shown in Fig. 3c. Each dot corresponds to a diode along the propagation axis. The gray and red dots correspond to pn-np and np-pn diodes connected to one transmission line, while the blue and green correspond to the pn-np and np-pn diodes connected the second transmission line having a $\pi/2$ phase difference. The achieved fundamental harmonic of the index modulation is shown in orange. One can clearly see that each modulation period λ_m of 450 μm is discretized in 4 parts, with period slightly reduced due to the traveling wave voltage distribution across the transmission line (green and gray dotted lines in Fig. 3c).

In our experimental structure, each diode is designed to be 110- μm long separated by a 2.5- μm region with the opposite dopant providing electrical insulation. Such choice of parameters ensures that the phase matching condition is satisfied at the operation frequency. The overall number of discrete modulation periods is 22, i.e. 88 modulation sections, or 166 diodes. In order to prevent the periodically-loaded transmission lines from having a cut-off below the desired modulation frequency we add spiral inductors in parallel with each of the pn-np and np-pn junctions in the waveguide (with a total length 1.5 mm corresponding to an $L \approx 1.84$ nH). The length of the stub connecting the capacitors and inductors to the transmission line also affects the cut-off frequency, and from design we expect that a 100- μm long stub would push the cut-off above 10 GHz. In order to induce maximum index modulation with minimal loss the dopant concentrations in the n-doped and p-doped regions were chosen to be $1 \times 10^{18} \text{cm}^{-3}$ and $1 \times 10^{17} \text{cm}^{-3}$ respectively, with the center of the doped region shifted about 190 nm from the center of each of the waveguides, so that losses are minimized for the index change required of the device.

We measure the forward and backward transmission spectra by inputting a continuous wave optical signal, applying a 10GHz modulation on the structure, and swapping the input and output fibers. Note that the amplitude of the output signal is not affected by the modulation since only the phase (i.e. refractive index) is modulated. Fig. 4 shows the ratio between the two spectra. When no electrical signal is applied the transmission is completely reciprocal with a unity contrast ratio between the forward and backward direction. (The noise measured in the experiments is caused by the mechanical instability of the coupling fiber and can be future reduced.) When the electrical signal is applied a clear dip appears in the spectrum, indicating nonreciprocity induced by photonic transition, as shown in Fig. 4. As we continue to increase the power of the applied modulation (i.e. stronger coupling between the even and odd modes), we obtain greater contrast between forward and backward transmission. We measured up to 3 dB contrast when operating at a wavelength of 1558 nm. This contrast is smaller than the one obtained from simulation due to limitations with our electrical signal power supply, which can achieve a maximum 25 dBm output power (or 5.6 V_p applied, which might be smaller due to reflections caused by impedance mismatch). For comparison we show in the bottom right of Fig. 4 the simulated relative transmission using the mode conversion equations and considering the dispersion of the waveguide to determine the bandwidth. One can see that the results agree well with the expected performance of the device.

The spectral width of the dip corresponds to the bandwidth of the device and is limited by the group velocity mismatch of the even and odd modes. In our measured spectrum (Fig. 4), we see significant non-reciprocity over a bandwidth of 200 GHz. This bandwidth is much larger than the modulation frequency used. This result provides a direct

experimental proof that the operating bandwidth of the device is not limited by the available modulation frequency, and thus a proof-of-principle demonstration that broadband operation of such a device is achievable. Theoretically, it has been pointed out that the bandwidth of such a device can exceed THz for 10GHz modulation frequency²⁴

Our demonstration of non-reciprocity provides an important step towards integrated non-magnetic optical isolator on a silicon chip. In addition to the bandwidth consideration as discussed above, the isolation ratio, insertion loss, and power efficiency of the device can be further improved using appropriate waveguide and electrical elements design and fabrication. The isolation ratio can be increased by having better impedance matching and higher input power for the electrical signal. There is no fundamental limit on the isolation ratio that one can obtain in the present scheme. For this specific device, the insertion loss is around 70dB primarily due to the waveguide scattering loss, which can be significantly reduced with better fabrication processes. Modulation loss caused by diodes will ultimately limit the insertion loss. In our current design, the dopants are expected to induce loss on the order of 16 dB for a 1.0 cm device. This loss could be decreased greatly by using alternative pn-junction schemes such as a recently demonstrated in²⁵, which also reduce the power consumption and increase the isolation attained. .

This work was performed in part at the Cornell NanoScale Facility, a member of the National Nanotechnology Infrastructure Network, which is supported by the National Science Foundation. This work was supported in part by the NSF through CIAN ERC under Grant EEC-0812072. Hugo Lira thanks his sponsorship support provided by the Brazilian Defense Ministry and insightful discussions with Prof. Ehsan Afshari. The

authors also acknowledge the support in part of the AFOSR-MURI program (Grant No. FA9550-09-1-0704).

Supplementary Information

We fabricate the device on a SOI platform in a completely CMOS-compatible process. The PMMA photoresist masks for the dopants are written using e-beam lithography, followed by implantation of B^+ with a concentration of $1 \times 10^{17} \text{cm}^{-3}$ and the P^- with a concentration of $1 \times 10^{18} \text{cm}^{-3}$. Masks for highly doped regions are written as well, followed by implantation of $1 \times 10^{20} \text{cm}^{-3}$ of BF_2^+ and Ar^- to form low resistance region for accessing the p and n regions, respectively, for electrical contacts. Next we write a maN-2403 photoresist mask with the waveguide pattern using e-beam lithography, and etched the silicon down 215 nm, leaving a thin 35-nm slab everywhere. The dopants are then activated on anneal furnace and RTA process, followed by cladding the waveguides with a 1- μm thick SiO_2 deposited with PECVD tool. We then write the mask for vias and inductors, etching through the SiO_2 and sputtering 100 nm of $MoSi_2$ for low resistance contacts and 600 nm of $AlCuSi$. Another cladding layer is deposited, 600-nm thick, and a second set of vias are etched. Finally, we write the mask for lift-off of a 1500 nm deposition of $AlCuSi$ to fill up the vias and form the transmission lines. In the left side of Fig. 4 we show an image of the electrical elements of the isolator (top) and of the optical elements (bottom) of the fabricated device. The insets point out to the inductors we place in parallel to the diodes, and to the vias which contact the pn-np diodes.

For the simulation shown in Fig. 2b, the input signal was set at a wavelength of 1550 nm, and the permittivity modulation has a maximum $\Delta\varepsilon=0.23211$, at 10 THz with wavenumber $q=541391 \text{ m}^{-1}$. The total length of the waveguide is $30\mu\text{m}$. Also, simulations with modulation frequency reduced down to 100 GHz were successfully performed, with $q=25984.8\text{m}^{-1}$, $\Delta\varepsilon=0.0182$ and device length of 0.413 mm, with mode conversion observed in only one direction. These parameters are chosen so that we can use full field simulations to highlight the essential physics, and to validate the coupled mode theory model. The experimental modulation frequency is at 10GHz, and the theoretical model that is directly compared to the experiments is a coupled mode theory model.

References:

1. Z. Yu, G. Veronis, Z. Wang and S. Fan, Phys. Rev. Lett. **100**, 023902 (2008).
2. F. D. M. Haldane and S. Raghu, Phys. Rev. Lett. **100**, 013904 (2008).
3. Z. Wang, Y. Chong, J. D. Joannopoulos and M. Soljacic, Nature **461**, 772 (2009).
4. S. Fan, R. Baets, A. Petrov, Z. Yu, J. D. Joannopoulos, W. Freude, A. Melloni, M. Popović, M. Vanwolleghem, D. Jalas, M. Eich, M. Krause, H. Renner, E. Brinkmeyer and C. R. Doerr, Science **335**, 38 (2012).
5. J. N. Winn, S. H. Fan, J. D. Joannopoulos and E. P. Ippen, Phys. Rev. B. **59**, 1551 (1999).
6. Z. Yu and S. Fan, Nat Photon **3**, 91 (2009).
7. K. Gallo, G. Assanto, K. R. Parameswaran and M. M. Fejer, Appl. Phys. Lett. **79**, 314 (2001).
8. M. Soljacic, C. Luo, J. D. Joannopoulos and S. H. Fan, Opt. Lett. **28**, 637 (2003).
9. S. K. Ibrahim, S. Bhandare, D. Sandel, H. Zhang and R. Noe, Electronics Letters **40**, 1293 (2004).
10. S. Manipatruni, J. T. Robinson and M. Lipson, Phys. Rev. Lett. **102**, 213903 (2009).
11. C. R. Doerr, N. Dupuis and L. Zhang, Opt. Lett. **36**, 4293 (2011).
12. L. Fan, J. Wang, L. T. Varghese, H. Shen, B. Niu, Y. Xuan, A. M. Weiner and M. Qi, Science **335**, 447(2012).
13. M. S. Kang, A. Butsch, and P. S. J. Russell, Nat. Photon. **5**, 549 (2011).
14. A. Kamal, J. Clarke and M. H. Devoret, Nat. Phys. **7**, 311 (2011).
15. J. Fujita, M. Levy, J. R. M. Osgood, L. Wilkens and H. Dotsch, Appl. Phys. Lett. **76**, 2158 (2000).
16. L. Bi, J. Hu, P. Jiang, D. H. Kim, G. F. Dionne, L. C. Kimerling and C. A. Ross, Nat. Photon. **5**, 758 (2011).
17. Y. Shoji, T. Mizumoto, H. Yokoi, I.-W. Hsieh and J. Richard M. Osgood, Appl. Phys. Lett. **92**, 071117 (2008).
18. W. Migaj, J. Romero-Vivas, B. Gralak, L. Magdenko, B. Dagens and M. Vanwolleghem, Opt. Lett. **35**, 568 (2010).
19. Z. Wang and S. Fan, Opt. Lett. **30**, 1989 (2005).
20. H. A. Haus, *Waves and fields in optoelectronics*. (Prentice-Hall, Englewood Cliffs, NJ, 1984).
21. S. E. Harris and R. W. Wallace, J. Opt. Soc. Am. **59**, 744 (1969).
22. P. Dong, S. F. Preble, J. T. Robinson, S. Manipatruni and M. Lipson, Phys. Rev. Lett. **100**, 033904 (2008).
23. Q. F. Xu, S. Manipatruni, B. Schmidt, J. Shakya and M. Lipson, Opt. Express **15**, 430 (2007).
24. Z. Yu and S. Fan, IEEE Journal of Selected Topics in Quantum Electronics **16**, 459 (2010).
25. A. Khilo, C. M. Sorace and F. X. Kärtner, Opt. Express **19**, 4485 (2011).

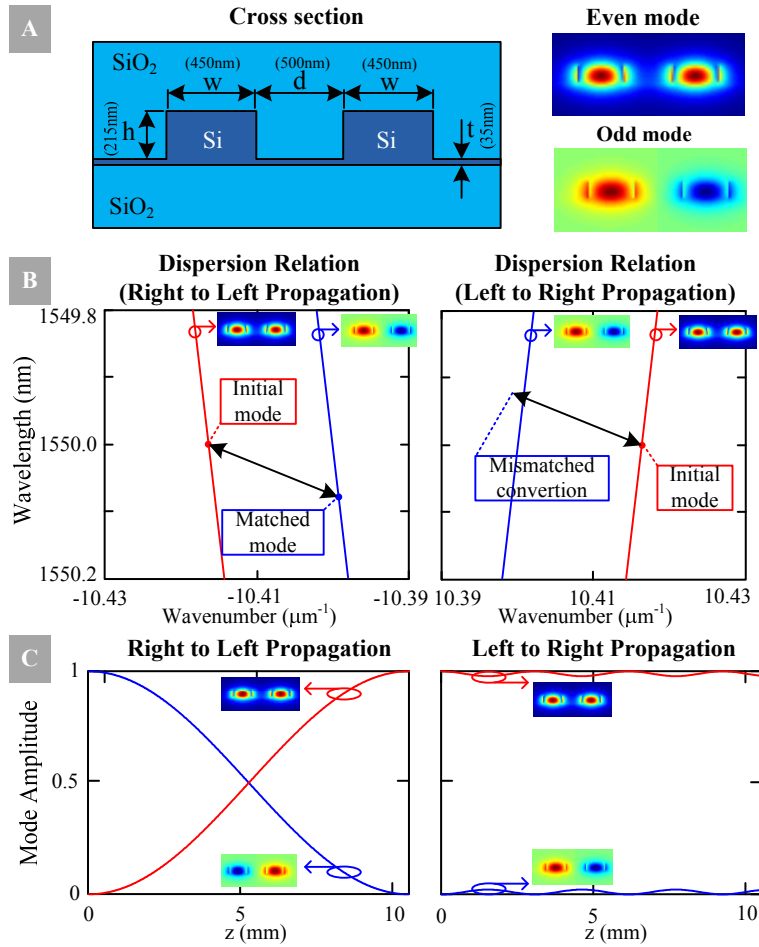


Fig. 1: (a) Waveguide geometry and materials. (b) Dispersion relation for even (red) and odd (blue) modes of coupled waveguides. The black arrow represents the traveling-wave index modulation. In the left, it matches the initial mode to another mode, while in the right it is observed conversion mismatch. (c) Dynamics of the mode conversion. Right to left propagation achieves full conversion from one mode to the other, while left to right propagation does not.

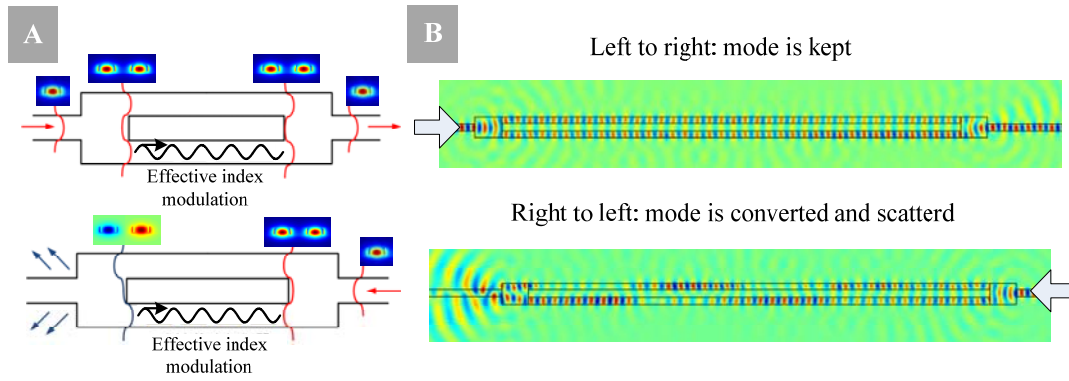


Fig. 2: (a) Schematic of the isolator. A single mode waveguide feeds a 1x2 MMI, which provides the even mode for the isolator. By modulating the refractive index of one waveguide we obtain a non-zero overlap between the modes and modulation. In one direction the even mode is converted to the odd mode, but it is not converted in the other direction. (b) FEM time-domain simulation showing the conversion occurring in only one propagation direction.

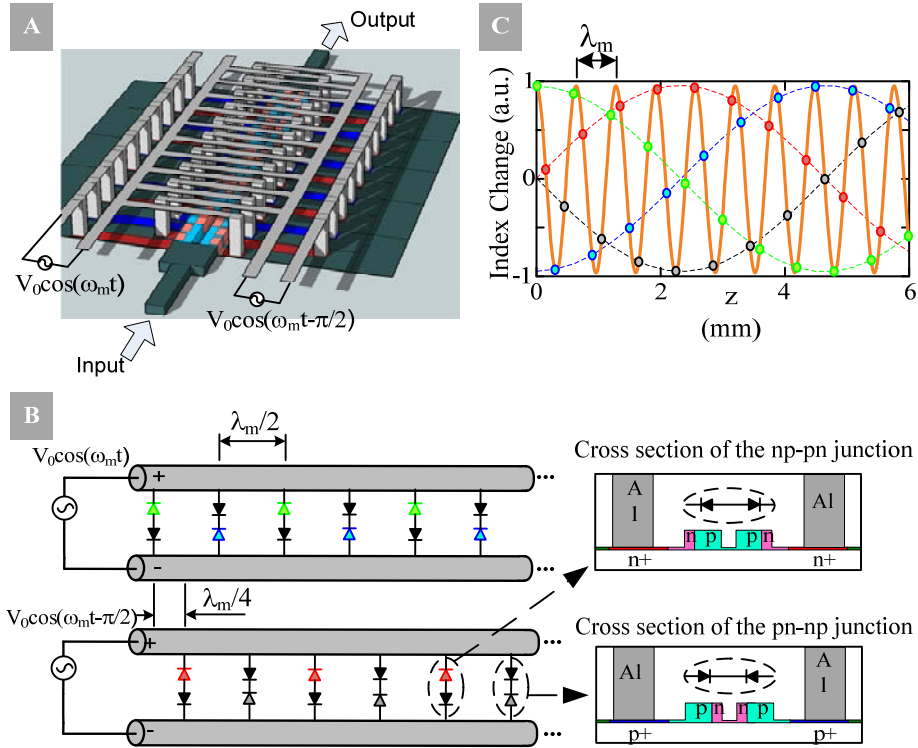


Fig. 3: (a) Simplified schematics of the device. Undoped silicon is shown in green, lightly p-doped silicon in light blue, lightly n-doped silicon in rose, heavily p-doped silicon in dark blue, heavily n-doped silicon in red, vias and electrical wiring in gray. (b) Schematics of the two transmission lines feeding pn-pn and np-pn junctions. Reverse biased diodes are represented in green, blue, red and gray while forward biased diodes are in black. The insets shown the distribution of dopants across the waveguide forming np-pn and pn-pn junctions. (c) Normalized index change. Each dot represent a diode in reverse bias along the waveguide. Green and blue dots are pn-pn and np-pn diodes fed by one transmission line, while red and gray are pn-pn and np-pn diodes fed by the delayed transmission line. In orange we have the fundamental harmonic of the discretized modulation achieved.

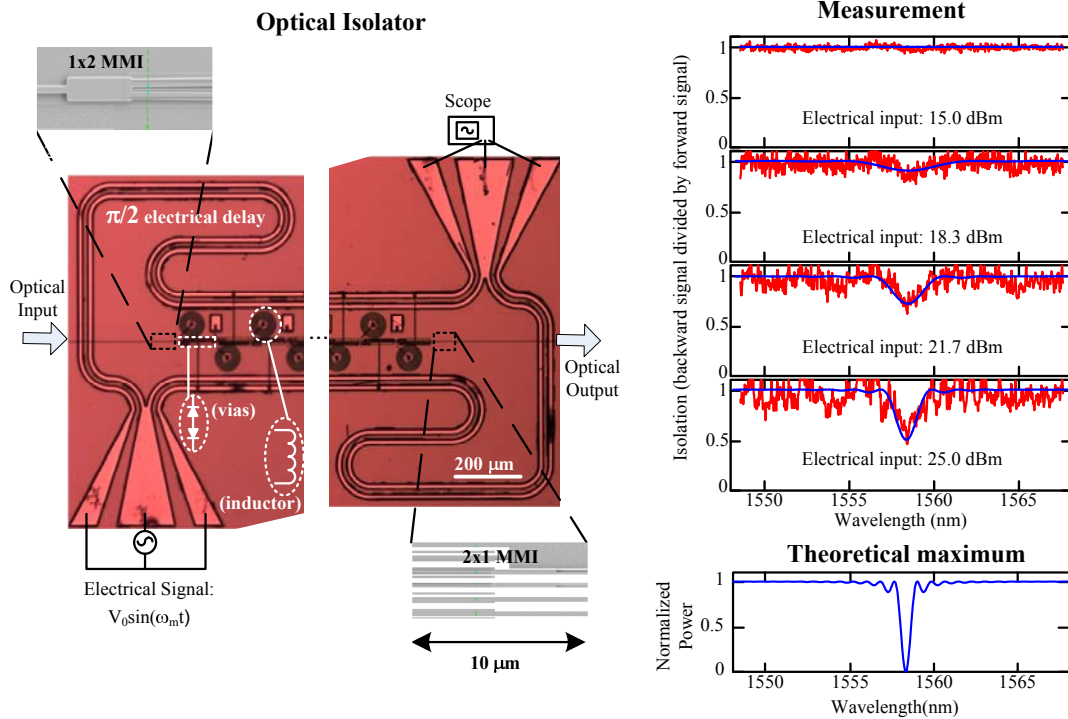


Fig. 4: In the left we show the electrical elements (Optical Microscope) and optical elements (Scanning Electron Microscopy) of the electrically-driven optical isolator. In the right we show sequentially the increase of isolation measured as a function of electrical signal input power (red). We observe up to 3 dB isolation with a electrical input of 25 dBm, and smaller values as the input decreases. The blue line is the fitting considering the conversion equations. In the bottom right we show the maximum isolation expected and the bandwidth of conversion for the dispersion extracted from the fitting of the measured data.

